Lateral proximity effect and long-range energy-gap gradients in Ta/Al and Nb/Al superconducting tunnel junctions

Roland den Hartog,[1] A. Golubov,[2] P. Verhoeve,[1] A. Poelaert,[1] D. Martin,[1] A. Peacock,[1] A. van Dordrecht,[1] and D. J. Goldie[3]

[1]*Astrophysics Division, Space Science Department of the European Space Agency, ESTEC, P.O. Box 299, 2200 AG Noordwijk, The Netherlands*

[2]*University of Twente, Department of Applied Physics, P.O. Box 217, 7500 AE Enschede, The Netherlands*

[3]*Oxford Instruments Scientific Research Division, Newton House, Cambridge Business Park, Cambridge CB4 4WY, United Kingdom*

(Received 14 August 2000; published 8 May 2001)

We present the results of current-voltage characterizations of Nb/Al and Ta/Al superconducting tunnel junctions, which reveal a dependence of the measured energy gap on the size of the junction. This implies a geometrical dependence of the energy gap, which suggests that the effective local energy gap has a lateral spatial variation on a scale of several μm. An extended version of the theory of the proximity effect could explain this phenomenon when lateral coherence lengths are introduced, which are of the order of the bulk coherence length in Al. One of the consequences of this theory is that the coherence length in a thin film cannot be taken to be isotropic. Another is that the effective lateral coherence length, which features in the lateral Usadel equation, actually depends on the quasiparticle energy.

DOI: 10.1103/PhysRevB.63.214507 PACS number(s): 74.50.+r

I. INTRODUCTION

When a superconducting material is brought into electrical contact with another (super)conducting material, Cooper pairs will diffuse across the interface between the materials, and the pair potential and the density of states on either side of the contact are influenced. As a consequence, the energy gap $\Delta_{\rm gap}$ is locally affected. This is usually referred to as the proximity effect.[1] The influence of the proximity effect on the coherent transport in normal-metal–superconductor contacts has been extensively studied both experimentally and theoretically in a number of recent publications.[2–12] With the advent of modern theoretical descriptions based on self-consistent solutions of either the Usadel equations or the Bogoliubov–de Gennes equations (see the reviews in Refs. 13–15), the proximity effect is now well enough understood to provide reliable predictions for the design of superconducting devices.[16,17] Examples of this ''energy-gap engineering'' are given in, e.g., Refs. 18 and 19. Up to now most treatments of the proximity effect have been strictly one dimensional: the variation of the local $\Delta_{\rm gap}$ is computed in the same (vertical) direction as in which the various layers of materials are stacked (see, however, Ref. 20). Through a stack of thin films (i.e., layer thickness of the order of the coherence lengths ξ) the gradient in $\Delta_{\rm gap}$ is essentially zero.[18] Quasiparticle trapping is then the result of differences in the density of states between the layers, resulting in Andreev reflections on the boundary between the materials. In a variety of applications, e.g., photon detectors with absorbers,[21–25] or arrays of junctions with high-Δ material bridges,[26] the proximity effect may extend over distances in excess of ξ in the lateral direction, and the problem will no longer be strictly one dimensional. In this paper the existing theory of the proximity effect is generalized for application to the two-dimensional problem of Nb/Al and Ta/Al superconducting tunnel junctions (STJ's) with an undercut at the edge, which locally suppresses the proximity of the Al on the Nb or Ta. This theory has two interesting implications. The first is that the local value of $\Delta_{\rm gap}$ may vary over distances that are substantially larger than the coherence length. The second is that when we reformulate the lateral variation in terms of Usadel's equation, an effective coherence length emerges, which is dependent on the quasiparticle energy.

II. EXPERIMENTS

A. Setup

The STJ's used in our experiments were fabricated by Oxford Instruments as part of an ongoing effort by the ESA to develop imaging spectroscopic detectors for astronomical purposes.[27,28] The sandwiches of Nb/Al/AlO$_x$/Al/Nb or Ta/Al/AlO$_x$/Al/Ta are magnetron sputtered in an Ar atmosphere on a superpolished sapphire substrate without breaking the vacuum in the deposition chamber. Deposition conditions are selected such that at least the first overlayer is epitaxial with the sapphire. The Al layer on Nb is always epitaxial, while the Al layers on Ta are polycrystalline once they are thicker than a few nm. Exposing the Al to a controlled amount of oxygen creates the AlO$_x$ barrier. The applied barrier recipe is always the same, resulting in a fairly constant barrier resistivity of $2.5\pm0.5\,\mu\Omega\,{\rm cm}^2$. The layers that are deposited on top of the barrier are always polycrystalline. The nominal layer thickness is 100 nm for the Nb and Ta base electrodes and 200 nm for the top electrode, but other combinations of electrode thickness have been used as well. The thickness of the Al layers in the Nb-based STJ's is in the range from 5 to 10 nm, while for the Ta devices it varies between 5 and 65 nm. The manufacturing process of the Nb-based STJ's is a modified version of the SNEP technique.[29,30]

 ©2001 The American Physical Society

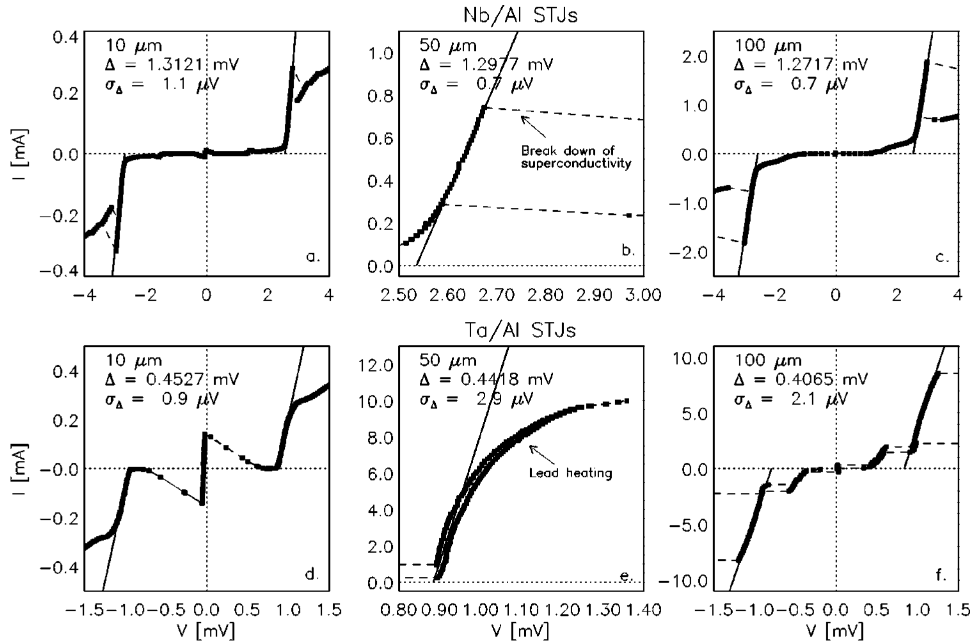

FIG. 1. Examples of $I(V)$ curves for STJ's of different sizes on the same chip. Solid markers indicate individual measured datapoints (V,I). The inset gives the values of the gap energy Δ_{gap} and its 1-σ formal error σ_Δ, estimated from linear least-squares fits to the flanks (solid lines). The top row shows an example of a chip with Nb/Al STJ's (sample 2 in Fig. 3 below), the bottom row a chip with Ta/Al STJ's (sample 6 in Fig. 3 below). Indicated in panel b is the point where the superconductivity breaks down. Panel e shows an example where the lead becomes resistive while the device remains superconductive. In this case the fit is made to the lowest part of the $I(V)$ curve. The consequences of these effects will be discussed further in Sec. IV C.

The base etch step is a standard wet etch in a solution of HF and HNO_3, tuned to etch Nb away as fast as Al. The Ta devices used in these experiments show a larger variation in base etch techniques, including wet etch techniques, reactive ion etching (RIE), and ion beam milling (IBM). So, whereas the series of Nb-based STJ's is quite homogeneous in layout, fabrication, and performance, the series of Ta STJ's shows larger variations. For the device patterning, standard photolithographic techniques were used to obtain two types of chips with Nb/Al STJ's. One type contains eight STJ's, with sizes of 20 and 50 μm, the other type contains ten STJ's with sizes in the range from 10 to 100 μm. This type of chip has also been used for the Ta/Al STJ's. Only sample 2 (of the ten we will discuss in some detail below) is an exception: this chip contains 200-μm STJ's as well.

The $I(V)$ curves are obtained in a standard way by scanning V_{bias} across the junction up and down and reading the current I at a temperature of 0.3 K. A magnetic field of up to a few 10 G was applied to suppress the Josephson current. We ensure, however, that this field did not influence the value of Δ_{gap}. The $I(V)$ curve is sampled with 400 measurements. The density of sampling increases with the gradient in the $I(V)$ curve to ensure good sampling statistics for the interesting features, such as the flanks. The gap voltages are determined at the intercept of a linear least-squares fit to the straight parts of the steep flanks in the $I(V)$ curves and the abscissa. The Δ_{gap} values for the STJ's are obtained from the gap voltages in the positive and negative part of the $I(V)$ curves as $\Delta_{\text{gap}}=\frac{1}{4}(V^+_{2\Delta}-V^-_{2\Delta})$. Examples of this procedure are given in Fig. 1, while the general setup of the electronics is shown in Fig. 2. Typically, Δ_{gap} can be determined with a 1-σ accuracy of (at worst) a few μV. This number follows from a standard error propagation analysis: $\sigma_\Delta=\frac{1}{4}[\sigma^2_+ +\sigma^2_-]^{1/2}$, where σ_+, and σ_- are the errors in the extrapolation of the fitted line $y=a+bx$ to the intercept with the abscissa (at $V=x_0$) on respectively the positive and negative side of the $I(V)$ curve. These errors are given by $\sigma^2_\pm=\sigma^2_a+2\sigma_{ab}x_0+\sigma^2_b x^2_0$, where σ_a, σ_b, and σ_{ab} are the standard errors in the fitted parameters a and b, and the covariance, respectively.[31]

B. Results

Figure 3 shows the results from Δ_{gap} measurements on four different samples of STJ's. This is a subset of a series of

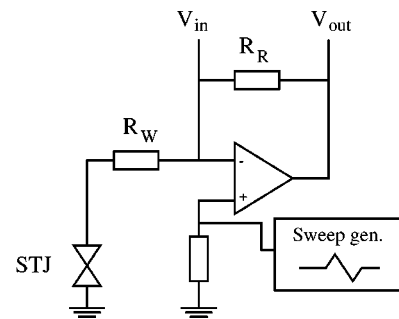

FIG. 2. Scheme of the electronics used for the current-voltage measurements. Each generated data point consists of a voltage pair V_{in} and V_{out}. The range resistor R_R is set to either 10 or 100 kΩ. The compensation for the wire resistance R_W is introduced in the software when V_{in} and V_{out} are translated to V and I.

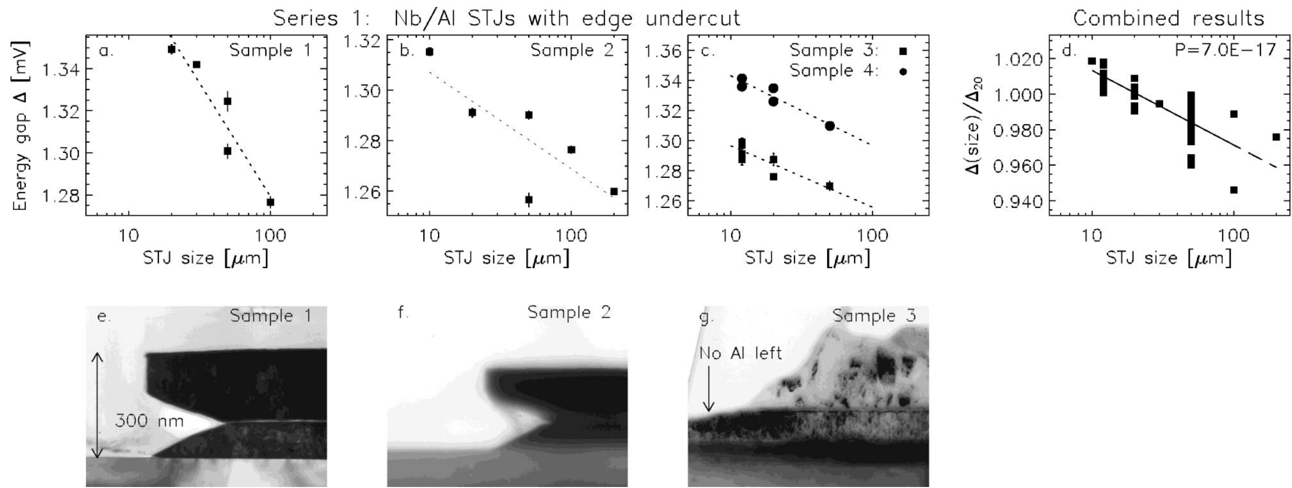

FIG. 3. (a)–(c) Gap energy Δ_{gap} as a function of junction size for four different chips with Nb/Al junctions with thin (5–10-nm) Al layers and undercut edges or Al missing from a part of the base Nb film. The bars indicate the 1-σ formal errors that result from the fitting procedure. (d) The results for 11 different chips combined. The gap energy was normalized to the value for an STJ size of 20 μm (that was present in all samples). The probability P for obtaining the observed (Spearman) correlation from a random distribution, (i.e., two-sided significance) is indicated in the inset. (e)–(g) TEM cross sections of an edge profile which is typical for these devices. An indication for the depth of the undercut is given.

11 different samples (with in total 54 junctions) with Nb/Al STJ's. The samples not shown mainly contain only 20- and 50-μm STJ's, but their data were used in the combined results in Fig. 3(d), and they account for most of the spread in the Δ_{gap} values at 20 μm. The dependence of Δ_{gap} on the size of the junctions is evident and highly significant, according to a standard nonparametric (Spearman) correlation test[31] applied to the combined data set. Because the comparison of STJ's with different sizes as shown in the individual panels in Fig. 3 is performed on the same chip, we can therefore safely exclude differences in fabrication routes or experimental circumstances as a possible cause for the Δ_{gap} variations. Differences in Δ_{gap} among STJ's with the same size that exceed the measurement errors indicate that the actual device patterning is a nonuniform process. They are the main source of scatter on the observed Δ_{gap}-size relation. As we will argue below, they are not responsible for the occurrence of this relation. This leaves spatial variation of the local Δ_{gap} in these junctions as the most probable explanation. The corresponding TEM cross-section images in Figs. 3(e) and (f) clearly show the undercut in the edge at the location of the Al layer, which we believe plays a central role in this effect. This undercut is an unintended by-product of the device patterning process. Apparently, the etching process during junction patterning is different from that during the simpler process development trials, resulting in a relative faster etching of the Al layer. Figure 3(g) shows a different edge profile with the same effect: instead of an undercut a part of the base Al layer with everything on top of it has been (again unintentionally) removed over a distance of about 300 nm. Figure 4 shows that the same effect is present in a series of three samples, comprising in total 28 Ta/Al junctions. The TEM images in Figs. 4(e)–(g) illustrate again how the etching process has affected the edge. Figure 5 demonstrates the physi-

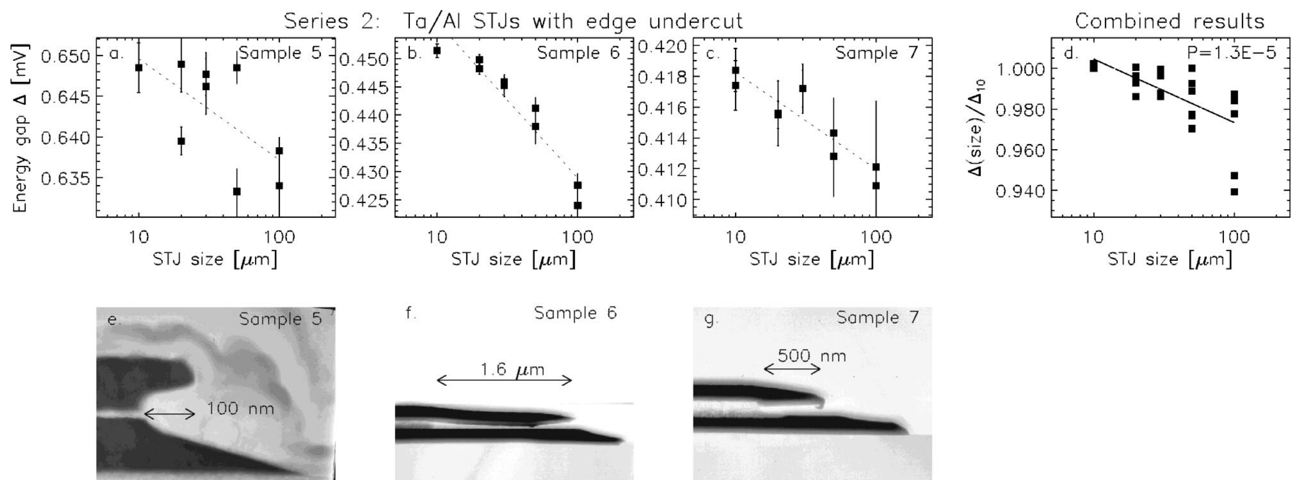

FIG. 4. As above, but now for Ta/Al junctions with Al layers of varying thickness (5–60 nm), and with varying undercut depth.

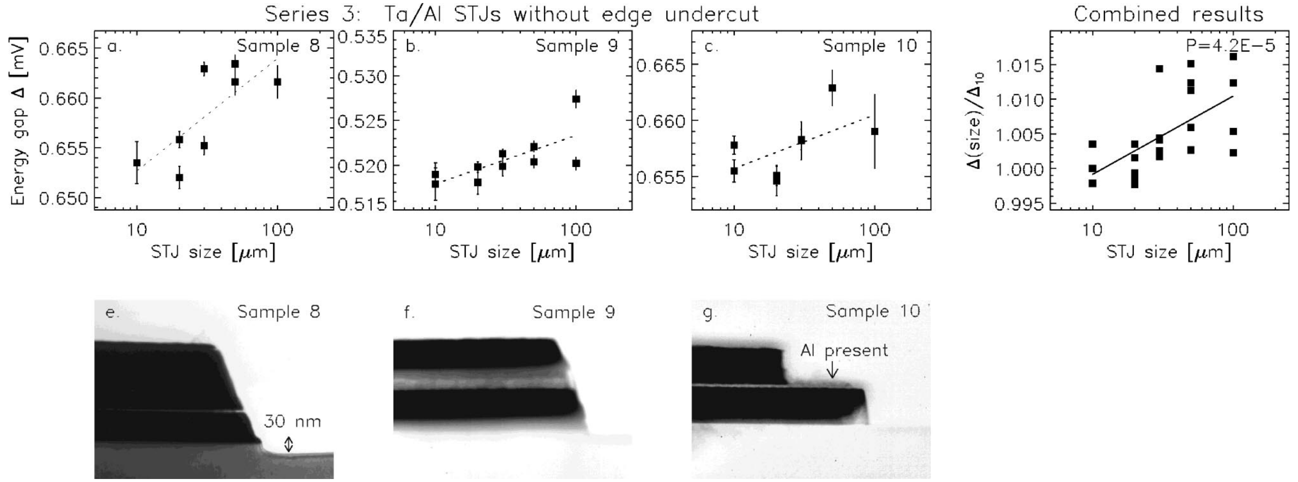

FIG. 5. As above, but now for Ta/Al junctions without an edge undercut.

cal link between the Δ_{gap} variation and the edge undercut with a third series, also of three samples, with in total 26 Ta/Al junctions, for which different patterning processes have been tried. This time, the corresponding TEM images in Figs. 5(e)–(g) show that the undercut in the edge is absent. Note that even in sample 10 [Fig. 5(g)], despite the absence of a part of the top electrode, the base Al layer covers the entire base electrode. At the same time we find that Δ_{gap} no longer decreases with increasing junction size. Figure 5(d) suggests that there is even a significant trend for the opposite effect. Therefore we have unambiguous proof of a physical link between the presence of the undercut and the spatial variation of Δ_{gap} with the size of the STJ's.

C. Interpretation

The Δ_{gap}-size relation strongly suggests a geometrical origin. A simple model based on two values for Δ_{gap} could already provide a qualitative explanation of the observed relation.[32] Suppose each STJ possesses a rim of fixed width in which Δ_{gap} is elevated, and a central area, which is larger for the bigger STJ's, where Δ_{gap} has its normal, proximized value. If the measured Δ_{gap} were some average over a distribution of local values of Δ_{gap}, then the measured Δ_{gap} would decrease for increasing STJ size. Now we associate the rim with a, say, 0.2-μm-wide region at the edge where the electrode material (Nb or Ta) is not in contact with the Al layer due to the undercut. As a consequence, the rim is not, or much less, proximized than the central region, which is in direct electrical contact with the Al. Because the bulk Δ_{gap} for Nb or Ta is higher than that of Al, the local value of Δ_{gap} in the unproximized rim will be higher than in the center. In its turn the rim of high Δ_{gap} material will influence the adjacent material with a lower value for Δ_{gap}. The proximity effect in this situation therefore has two spatial dimensions. Figure 6 provides a sketch of this situation. A comparison among the individual samples of series 2 in Fig. 4 indicates that the strength of the effect, defined as the slope of the relation between Δ_{gap} and size, does not depend on the depth of the undercut. A comparison between series 1 and 2, on the other hand, strongly suggests a dependence on the electrode material: for Nb the effect seems three times stronger than for Ta. For the samples in series 3, Ta/Al STJ's without undercut, Fig. 5 provides an indication of the converse situation. Here the energy gap actually *increases* with increasing STJ size. These STJ's were patterned using the IBM technique. The TEM image of sample 8 shows clearest how ~30 nm of the sapphire outside the STJ has been removed during IBM. Another consequence of IBM, which is not readily visible in the TEM image, is localized damage to the Ta lattice close to the edge. Upon impact, ricocheting ions will dislocate atoms in the lattice close to the edge, and constitute impurities. It is well known that the critical temperature depends both on impurity content (the isotope effect) and the quality of the lattice. Both dislocations and impurities will tend to locally decrease T_C, and thus the local energy gap. So, in the samples of series 3, we indeed expect an opposite effect by the above mechanism, resulting in an increasing energy gap measured for STJ's with increasing sizes.

III. TWO-DIMENSIONAL PROXIMITY EFFECT

The introduction of a second spatial dimension in the proximity problem, in order to compute lateral variations in Δ_{gap}, requires several modifications of the approach outlined

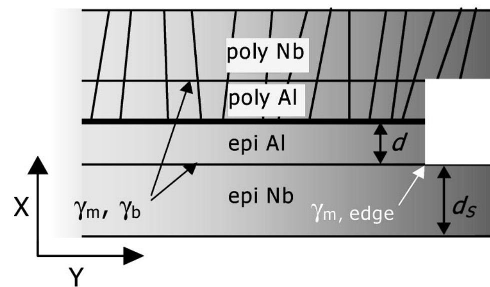

FIG. 6. Schematic representation of a cross section of a Nb/Al STJ with an edge undercut, illustrating the two-dimensional aspects of the proximity effect. The greyscale indicates the local value of the energy gap: the darker the color, the higher Δ_{gap}. The width of the Al layer has been exaggerated for clarity. See Sec. III for further details.

in Ref. 16. First, the introduction of a lateral (clean limit) coherence length ξ_y with a corresponding term in the Usadel equations is needed, in addition to the usual vertical (dirty-limit) coherence length ξ_x. In two dimensions Eqs. (3) and (4) of Ref. 16, which describe the Al interlayer, then become

$$\Phi=\Delta+\frac{\pi T_c}{\omega G}\left\{\xi_x^2\frac{\partial}{\partial x}\left[G^2\frac{\partial}{\partial x}\Phi\right]+\xi_y^2\frac{\partial}{\partial y}\left[G^2\frac{\partial}{\partial y}\Phi\right]\right\}, \tag{1a}$$

$$\Delta\ln\frac{T}{T_c^*}+2\pi T\sum_{\omega>0}\frac{\Delta-G\Phi}{\omega}=0, \tag{1b}$$

$$G=\frac{\omega}{\sqrt{\Phi^2+\omega^2}}. \tag{1c}$$

Here Δ is the pair potential (not the energy gap!) and Φ is a function related to G via Eq. (1c), but without a direct physical meaning. Note that for reasons of clarity $\hbar$ and k are set to unity. T_C^* is the critical temperature of the Al layer. In these equations the central role is played by the complex Green's function G, which is a function of energy ε and position (x,y). It is directly related to the density of states of the quasiparticles (QP's) and Cooper pairs (CP's):

$$N_{\mathrm{QP}}(\varepsilon,x,y)=\mathrm{Re}\,G, \tag{2a}$$

$$N_{\mathrm{CP}}(\varepsilon,x,y)=\mathrm{Re}\,G\Phi/\omega. \tag{2b}$$

Implicit in these equations is the relation between the real energy ε and the Matsubara frequency $\omega_n=\pi T[2n+1]$ ($n=0,1,2,...$): $\varepsilon=-i\omega_n$. For each layer, a separate set of equations of the form (1a)–(1c) is required, plus a set of boundary conditions for each interface.

Below we will consider only bilayers of Al with Nb and Ta, in which the Al layer is the most important for tunneling processes. Since it is adjacent to the barrier on both sides, all the tunneling takes place to and from this layer. The thickness of the Al layer is generally small, $d\ll\xi_x$, due to the large value of the bulk coherence length ($\xi_{\mathrm{bulk,Al}}=1.6\,\mu$m). The other layer (Nb or Ta), indicated by subscript S, controls the lateral proximity effect. It is usually thicker, $d_S\approx\xi_{x,S}$. Conform Ref. 16, the domain $-d\leqslant x<0$ is occupied by the Al layer, and $x\geqslant 0$ by the S layer. The input parameters of Eqs. (1a)–(1c) describe the boundary conditions between the S and the Al layer. Far away from the edge (at $y=\infty$), the value of γ_m (associated with the density of states on either side of the interface) and γ_B (associated with the transmissivity of the interface) are the same as in the one-dimensional case discussed in Ref. 16:

$$\gamma_m=\frac{\rho_s\xi_{x,S}}{\rho\xi_x}\frac{d}{\xi_x}=\sqrt{\frac{D}{D_S}}\frac{N_S(0)}{N(0)}\frac{d}{\xi_x}=\gamma\frac{d}{\xi_x}, \tag{3a}$$

$$\gamma_B=\frac{R_B}{\rho\xi_x}\frac{d}{\xi_x}=\gamma_{\mathrm{BN}}\frac{d}{\xi_x}. \tag{3b}$$

The definitions γ, γ_{BN} are used to remain compatible with other work in this field.[18,33] Here ρ is the normal-state resistivity of the metal, R_{B} is the product of the barrier resistance and the area, and $\xi=[D/2\pi T_C]^{1/2}$ is the (dirty-limit) coherence length, with T_c the critical temperature in the S layer. The value of γ_m determines the strength of the coupling between the S and the Al layer, while γ_B determines the electrical contact. The right-hand side of Eq. (3a) is based on the relations between ξ and the normal-state diffusion coefficient D, and between the normal-state resistivity and normal-state single-spin density of states, $\rho=[e^2DN(0)]^{-1}$ (see Ref. 16). This demonstrates the link between γ_m and the ratio of the normal-state density of states $N(0)$ on either side of the S/Al interface.

Strictly speaking, when for a finite thickness of the Al layer the condition $d\ll\xi_x$ is not fulfilled, the boundary conditions depend on parameters γ, γ_{BN}, and d separately.[18,33] Still, as is shown in Ref. 18, the parametrization in Eqs. (3a) and (3b) is accurate up to terms of second order in d/ξ_x. In practice this approximation works rather well; e.g., the error is within 5% when $d<0.5\xi_x$. In the present case we are certainly in the regime where $d\ll\xi_x$, therefore it is more convenient to use the parametrization in γ_m and γ_B, which we will maintain in the discussion below. An additional boundary condition at the undercut edge follows from an analysis of the derivation of the boundary conditions in Ref. 34:

$$\gamma_{m,\mathrm{edge}}=\gamma_m/2, \tag{4a}$$

$$\gamma_{B,\mathrm{edge}}=\gamma_B. \tag{4b}$$

Equation (4a) indicates that the number of states in the Al layer available to normal-state electrons in the S layer is halved due to the undercut. This boundary condition is independent of the depth of the undercut, which is in agreement with the results obtained for series 2. Equation (4b) implies that at the edge we do not expect a change in the properties of the interface between the Al and S layers. Separating x and y in Eq. (1a) and replacing ω by $i\varepsilon$ gives for the Al layer

$$i\xi_x^2\frac{\pi T_c}{\varepsilon G}\frac{\partial}{\partial x}\left(G^2\frac{\partial}{\partial x}\Phi\right)=\Phi-\Delta-i\xi_y^2\frac{\pi T_c}{\varepsilon G}\frac{\partial}{\partial y}\left(G^2\frac{\partial}{\partial y}\Phi\right). \tag{5}$$

As mentioned above, we consider here the case of small interlayer thickness. This allows further simplification of the problem. Since $d\ll\xi_x$, the functions G and Δ are in first approximation independent of x. Thus the problem of the two-dimensional proximity effect is essentially reduced to the solution of a one-dimensional equation. Integration of Eq. (5) then yields

$$i\xi_x^2\frac{\pi T_c G}{\varepsilon(x+d)}\frac{d}{dx}\Phi=\Phi-\Delta-i\xi_y^2\frac{\pi T_c}{\varepsilon G}\frac{d}{dy}\left(G^2\frac{d}{dy}\Phi\right). \tag{6}$$

Such an approach was used by Kupriyanov[20] in order to treat a two-dimensional proximity effect in SNS microbridges with variable thickness. The boundary condition on the interface of the Al layer with the barrier is

$$\frac{\partial}{\partial x}\Phi(x=-d)=0. \tag{7a}$$

Combining with the boundary condition at the S/Al interface,

$$\gamma_B\frac{\xi_x^2}{d}G\frac{\partial}{\partial x}\Phi(x=0)=G_s(\Phi_s-\Phi), \tag{7b}$$

yields

$$(G_s-i\gamma_B\tilde{\varepsilon})\Phi=G_s\Phi_s-i\gamma_B\tilde{\varepsilon}\tilde{\Delta}+\frac{\xi_y^2}{G}\frac{\partial}{\partial y}\left(G^2\frac{\partial}{\partial y}\Phi\right), \tag{8}$$

where $\tilde{\varepsilon}=\varepsilon/\pi T_c$, $\tilde{\Delta}=\Delta/\pi T_c$.
Finally, we introduce, cf. Ref. 16, functions θ and θ_S such that $G=\cos\theta$, $\Phi=-i\varepsilon\tan\theta$, $G_S=\cos\theta_S$, and $\Phi_S=-i\varepsilon\tan\theta_S$ to arrive at the following basic equation for the variation of θ along the y direction:

$$\frac{\partial^2\theta}{\partial y^2}+\left(\tilde{\Delta}+\frac{\sin\theta_s}{\gamma_B}\right)\cos\theta+\left(i\tilde{\varepsilon}-\frac{\cos\theta_s}{\gamma_B}\right)\sin\theta=0. \tag{9}$$

This equation governs the variations of the density of states along the y direction in the Al layer, through Eqs. (2a) and (2b). In the bulk superconductor, θ_S is given by $\theta_S=\tan^{-1}(i\Delta_S/\varepsilon)$, where Δ_S is the bulk pair potential in S. Equation (9) has a form similar to the Usadel equation in a superconductor with an effective pair potential $\tilde{\Delta}_{\rm eff}=\tilde{\Delta}+\gamma_B^{-1}\sin\theta_s$ and an effective energy $\tilde{\varepsilon}_{\rm eff}=\tilde{\varepsilon}+i\gamma_B^{-1}\cos\theta_S$. Here θ_S $(x=0)$ is the solution of the Usadel equations in the y direction, taken at the interface between the Al and S layer. Equation (9) can be cast in the form

$$\xi_{\rm eff}^2\frac{\partial^2\theta}{\partial y^2}\sin(\theta+C)=0, \tag{10a}$$

where C is a constant (the actual expression for C is not relevant here), while $\xi_{\rm eff}$ is given by

$$\frac{\xi_{\rm eff}}{\xi_y}=\left[\tilde{\Delta}^2-\tilde{\varepsilon}^2+2\frac{\tilde{\Delta}\sin\theta_s-i\tilde{\varepsilon}\cos\theta_s}{\gamma_B}+\frac{1}{\gamma_B^2}\right]^{-1/4}. \tag{10b}$$

Equation (10a) implies that $\xi_{\rm eff}$ determines the length scale of the spatial variation of θ at a given quasiparticle energy. It follows from Eq. (10b) that $\xi_{\rm eff}$ has a pole at an energy

$$\tilde{\varepsilon}_g=i\frac{\cos\theta_s}{\gamma_B}+\sqrt{\frac{\sin^2\theta_s}{\gamma_B^2}+2\frac{\tilde{\Delta}\sin\theta_s}{\gamma_B}+\tilde{\Delta}^2}, \tag{10c}$$

which corresponds to the gap energy in the Al layer. Thus, for quasiparticle energies close to the gap, the effective coherence length is enhanced compared to ξ_y. Although this effect is not very strong, because of the $\frac{1}{4}$ power, it is a remarkable feature. The same also holds for a bulk superconductor, where $\xi_{\rm eff}=\xi_S[\tilde{\Delta}_S^2-\tilde{\varepsilon}^2]^{-1/4}$. This follows directly from Eq. (10b) by setting $\gamma_B^{-1}=0$ and $\Delta=\Delta_S$. The boundary conditions for Eq. (9) at the edge $(y=0)$ and far away from the edge $(y=\infty)$ are expressed via the solution of the proximity effect problem in the x direction at the Al/S interface θ_S at $x=0$:

$$\tan\theta(y=0)=\frac{\gamma_B\tilde{\Delta}+\sin\theta_S(x=0,y=0)}{-i\gamma_B\tilde{\varepsilon}+\cos\theta_S(x=0,y=0)}, \tag{11a}$$

$$\tan\theta(y=\infty)=\frac{\gamma_B\tilde{\Delta}+\sin\theta_S(x=0,y=\infty)}{-i\gamma_B\tilde{\varepsilon}+\cos\theta_S(x=0,y=\infty)}. \tag{11b}$$

Equation (9) is now solved along the y direction with the boundary condition (11a) and (11b), cf. the methods outlined in Ref. 16. The first step is the selection of a parameter set (γ_m,γ_B) for our model. We emphasize here that the exact values of γ_m and γ_B are not of primary importance for the present study. They serve only as a starting point for our discussion of the long-range lateral proximity effect in Al. Several examples of Nb/Al and Ta/Al structures were considered in Ref. 18, which are of a quality that is comparable to that of the STJ's in this study. It was shown that in all cases the ratio $\gamma_{\rm BN}/\gamma$ is close to 2 for the Nb/Al combination. Thus we took $\gamma_B/\gamma_m=\gamma_{\rm BN}/\gamma=2$ also in the current case. The remaining adjustable parameter is then fixed by the measured gap reduction in the STJ. In this way we obtain $\gamma_m=0.3$ and $\gamma_B=0.6$, in reasonable agreement with the results in Ref. 18. Zehnder *et al.*[33] also determined the $\gamma_{\rm BN}$ and γ parameters for a series of Nb/Al STJ's, but arrive at quite different values, presumably due to substantial differences in layup and fabrication between their devices and ours. For the Ta/Al structure we derived $\gamma_m=0.1$ and $\gamma_B\approx0.3$, which corresponds to an average of the results in series 2.

The key output from the above model is the density of quasiparticle states in the lateral direction, $N_{\rm QP}(\varepsilon,y)$, close to the barrier. Figures 7(a) and (b) show $N_{\rm QP}(\varepsilon,y)$ in a Nb/Al bilayer, close to the barrier $(x=-d)$ as a function of distance to the edge, and as a function of quasiparticle energy, respectively. For quasiparticle energies close to the gap the distance over which $N_{\rm QP}(\varepsilon,y)$ varies may be as large as $10\xi_y$, as can be seen in Fig. 7a. This amplification of the proximity range is essential to understanding how a feature at the edge can influence the measured energy gap of an STJ as large as 50 μm. Clearly, the distance from the edge at which $N_{\rm QP}(\varepsilon,y)$ saturates depends on quasiparticle energy, a consequence of $\xi_{\rm eff}$ depending on quasiparticle energy as discussed above. Figure 7(b) shows another important feature: in all curves quasiparticle states exist down to energies 1.24 meV, but the number of states is a strong function of position. Figures 7(a) and (b) thus demonstrate that in two-dimensional proximized superconductors the definition of the energy gap becomes to some extent arbitrary.

IV. APPLICATION TO CURRENT-VOLTAGE CHARACTERISTICS

A. Construction of $I(V)$ curves

From the results shown in Fig. 7(b), the density of quasiparticle states $N_i(\varepsilon,\mathbf{y})$, in both electrodes as a function of

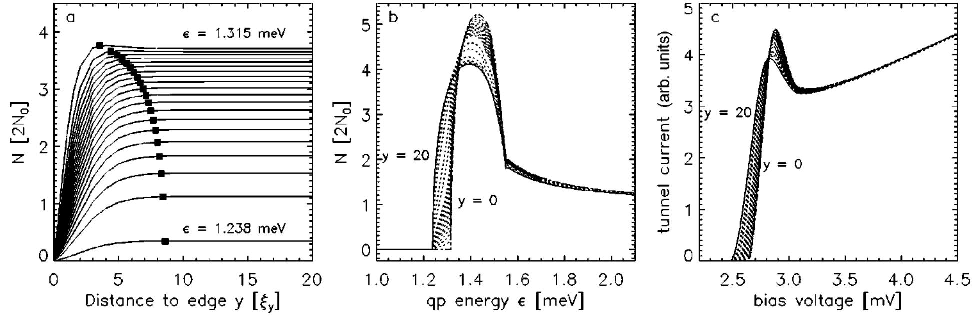

FIG. 7. The basic results of the two-dimensional proximity model for a Nb/Al bilayer with $\gamma_m = 0.3$ and $\gamma_B = 0.6$: the density of quasiparticle states $N(\varepsilon,y)$, measured in units of $2N_0$. Vertical positions are chosen close to the barrier $(x=-d)$. (a) $N_{\mathrm{QP}}(\varepsilon,y)$ as a function of distance to the edge y for various quasiparticle energies. The squares indicate the distance at which the density of states ''saturates.'' (b) $N_{\mathrm{QP}}(\varepsilon,y)$ as a function of quasiparticle excitation energy ε. Curves are shown for $y \in [0, 0.1, 0.2,...,1, 1.5, 2, 3,...,10, 20]$ in units of the lateral coherence length ξ_y. (c) The corresponding tunnel currents, in the case of $N_{\mathrm{QP}}(\varepsilon,y)$ for various values of y on one side of the barrier and $N_{\mathrm{QP}}(\varepsilon,20\xi_y) \approx N_{\mathrm{QP}}(\varepsilon,\infty)$ on the other side.

(two-dimensional) position $\mathbf{y}$, can be readily determined, provided we know the effective lateral coherence length in both electrodes. Individual tunnel currents $I_{SS}(V,\mathbf{y})$ are then obtained using the familiar expression (see, e.g., Ref. 35)

$$I_{SS}(V,\mathbf{y}) = \frac{G_{nn}}{e}\int_{-\infty}^{+\infty} d\varepsilon [f(\varepsilon) - f(\varepsilon + eV)] \times \frac{N_1(\varepsilon,\mathbf{y})}{N_1(0)} \frac{N_2(\varepsilon + eV,\mathbf{y})}{N_2(0)}, \tag{12}$$

where G_{nn} is the normal-state conductivity of the STJ. In Fig. 7(c) examples of tunnel currents are shown, arising between a region with $N_1(\varepsilon,\mathbf{y})$, for various values of $\mathbf{y}$, on one side of the barrier and $N_2(\varepsilon,\infty)$ on the other side. The sharp rise in the tunnel current near the gap energy is caused by the sudden possibility for members of Cooper pairs on one side of the barrier to individually tunnel into quasiparticle states on the other side of the barrier. Because the member that stays behind also becomes a quasiparticle, the tunnel current is actually governed by the density of quasiparticle states on either side of the barrier, hence the appearance of N_1 and N_2 in Eq. (12).

B. Measurement of the energy gap

The elevation of the local energy gap close to the edge implies that there is a range of bias voltages, $2\Delta_{\mathrm{center}} < eV_{\mathrm{bias}} < 2\Delta_{\mathrm{edge}}$, for which quasiparticles can tunnel into the central region of the electrode, but not into the rim close to the edge. The electrical circuit is closed when the quasiparticles undergo Andreev reflections from the rim, thereby emitting Cooper pairs into the rim. This situation is analogous to that in the experiments discussed by Clarke and Tinkham.[36,37] They concluded that when a quasiparticle current is converted into a pair current, the quasiparticle potential in the nonequilibrium region differs from the pair chemical potential μ_p by a value eV_{QP}. Below we argue that this value is proportional to the area of the region in which the tunneling takes place and of sufficient magnitude to drive down the effective gap in the adjacent region to a level that tunneling will take place there as well. The consequence is that the STJ is driven towards a situation in which the tunnel current is uniform across the surface, at the expense of local variations in the quasiparticle potential (with respect to the level set by the bias voltage). This implies that the integration over the barrier area of the local $I(V)$ curves in Fig. 7(b) should take place in horizontal direction (i.e., for fixed values of tunnel current density) instead of in the vertical direction (for fixed values of the bias voltage):

$$V(I) = \int_{\mathrm{area}} d\mathbf{y} V(I,\mathbf{y}). \tag{13}$$

This computation requires the inversion of Eq. (12) with respect to V, an operation that is easily performed numerically.

Because of the high bias voltage, the quasiparticles that tunnel into the central region have a strong electronlike (or holelike) character. This results in a local branch imbalance, which is characterized by the quantity $Q = n_e - n_h$, where n_e, n_h are the densities of electron- and holelike quasiparticles, respectively. Tinkham and Clarke concluded that the value eV_{QP} is proportional to the quasiparticle current I:

$$\mu_{\mathrm{QP}} - \mu_p = eV_{\mathrm{QP}} \approx Q/2N(0)g \approx I\tau_Q/2e\Omega N(0)g, \tag{14}$$

where τ_Q is the branch-mixing time, i.e., the time it takes Q to relax to zero, g is the conductance of the interface across which V_{QP} develops, and Ω is the volume of the superconductor. This expression is valid for all temperatures, provided the temperature dependence of τ_Q is taken into account. Since the quasiparticle current I is proportional to the area of the barrier, so is V_{QP}. Our situation differs on two minor points from the one for which Eq. (14) was derived. In our case, the quasiparticle current is converted into a pair current by Andreev reflections against the surrounding region with elevated Δ, instead of by tunneling from a normal metal into a superconductor. As a result, the normalized (tunnel) conductivity g_{NS} in the analysis by Tinkham and Clarke must be replaced by a factor $g=2$ for Andreev reflections (see, e.g., Ref. 34). Also, our experiments were carried out at a much lower temperature. Therefore inelastic scattering and Andreev reflections may compete as the dominant process

for branch mixing. For the energy range indicated in Fig. 7(b) [taking $\Delta(0)=1.24\,\mathrm{meV}$, $\varepsilon_{\max}=1.32\,\mathrm{meV}$), the inelastic τ_Q in the low-T limit[38] is at least 2.4 μs, but for energies $\Delta(0)<\varepsilon\ll\varepsilon_{\max}$ it is much larger. For the Nb/Al STJ's in our sample, diffusion constants D were estimated to be 130 $\mathrm{cm^2\,s^{-1}}$ for the base electrode and 7 $\mathrm{cm^2\,s^{-1}}$ for the top electrode,[39] equivalent to diffusive crossing times of 0.1 and 1.8 μs for, respectively, the base and top electrode of a 50×50-$\mu\mathrm{m}^2$ STJ. These values are based on the familiar relation $D=\frac{1}{3}\langle v_{\mathrm{QP}}\rangle l$, where the mean-free path l is based on measurements of the residual-resistance ratio of the films, and the mean quasiparticle velocity $\langle v_{\mathrm{QP}}\rangle$ includes the usual low-energy correction with respect to the Fermi velocity.[40] However, recent work bears out growing evidence that quasiparticles diffuse considerably slower (typically a factor 5–7) than this relation predicts.[21,22,41,42] In, for example, a 50-μm Nb/Al STJ we expect a current I of 25 mA for a bias of 2.5 mV, which would result in a V_{QP} of 0.5 mV, if we assume a short τ_Q of 0.1 μs. This is more than enough to bridge the gap difference of ~0.1 mV between the center and edge. In Fig. 1 we see that due to the breakdown of superconductivity, the actual current may be a factor 30 smaller. Even with such a low current it is possible to obtain a V_{QP} of 0.1 mV in the base electrode when the actual quasiparticle diffusion is indeed a factor of 6 slower.

C. Breakdown of superconductivity in the leads

Figure 1 shows another geometrical dependence of the $I(V)$ characteristics. For sample 1, the maximum current measured near the gap voltage is roughly a linear function of STJ size, instead of a linear function of area as one would expect from Eq. (12), and as one can see in the data for sample 6 in Fig. 1. Consider a scan, increasing in V_{bias}, across the gap voltage. At the maximum current, there is a sudden change in the impedance of the STJ, which causes the jump in the $I(V)$ curve. We interpret this jump in terms of a breakdown of superconductivity somewhere in the superconducting circuit. Inspection of the sample data reveals that the effect is specific for samples 1 and 2. It is probably related to the crystallographic quality of the leads. A flaw somewhere then drastically reduces the maximum current that can flow through the region before it becomes normally conducting. Once part of the circuitry becomes normally conducting, heat is generated and the local temperature rises probably quickly above T_c. In particular the top lead, which is deposited after the device patterning process, may be susceptible to such problems. A clear example of the heating process is shown in Fig. 1(e). The curvature clearly deviates from what is expected for a normal $I(V)$ curve, and is consistent with an increasing serial resistance. During this scan the sample temperature increased from 0.32 to 0.45 K. In this case, however, a complete breakdown of the superconductivity did not occur. But, as is clear from Fig. 1(e), the heating effect does limit the part of the curve to which a reliable fit can be made. In either case, the net result is a progressively lower cutoff in the current, which promotes an artificial decrease of the measured energy gap (see Fig. 8).

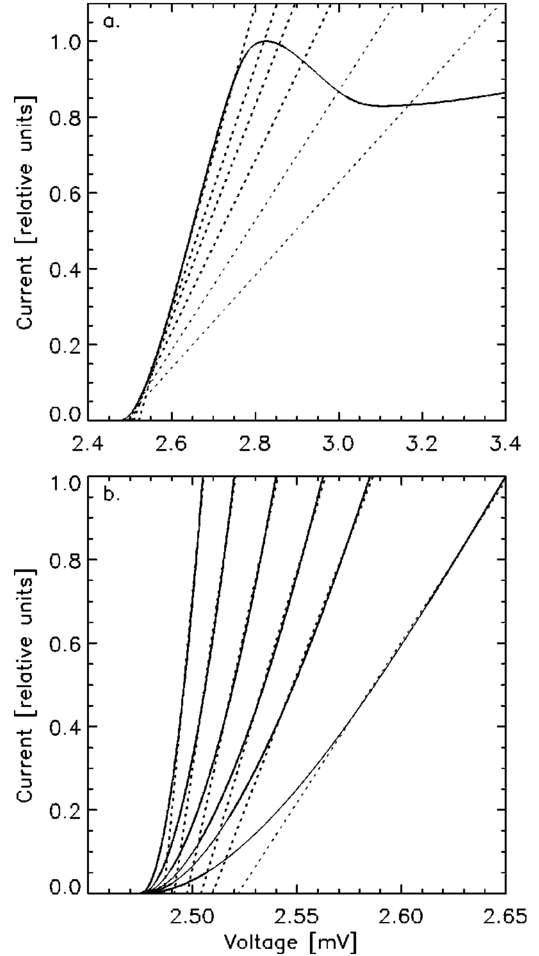

FIG. 8. Illustration of how the breakdown of superconductivity in the leads of the STJ at decreasing current levels influences the measurement of the energy gap. (a) Full $I(V)$ curve, (b) blowup, scaled to the maximum current level for each fit.

D. Comparison between model and data

Figures 9(a) and (b) show the results of a simulation of the data for the Nb/Al STJ's, as displayed in Fig. 3. The two main input parameters, $\gamma_m=0.3$ and $\gamma_B=0.6$, are typical of Nb STJ's with thin (5-nm) Al layers. These computations separate the different factors discussed above. The main conclusion is that it is possible to quantitatively explain the observed Δ_{gap}-size relation. Furthermore, it is clear that this relation cannot be solely explained as the result of an artifact, such as the breakdown of superconductivity for some current. So there really is an important contribution from the lateral proximity effect. An essential assumption is the value of the lateral coherence lengths ξ_y on either side of the barrier. In the case of the Nb/Al STJ's they are different because the Al in the base electrode is epitaxial with the Nb, while in the top electrode the Al is polycrystalline, with a typical size for the crystallites of 50 nm. In order to explain the full range of measured gap energies in Fig. 3, rather extreme values for ξ_y in the Al layers must be assumed on either side of the barrier, namely $\xi_y\approx1.6\,\mu\mathrm{m}$ on the epitaxial side and $\xi_y\approx0.5\,\mu\mathrm{m}$ on the polycrystalline side ($\xi_{\mathrm{bulk,Al}}=1.6\,\mu\mathrm{m}$). Substantially smaller values on either side do not suffice, as

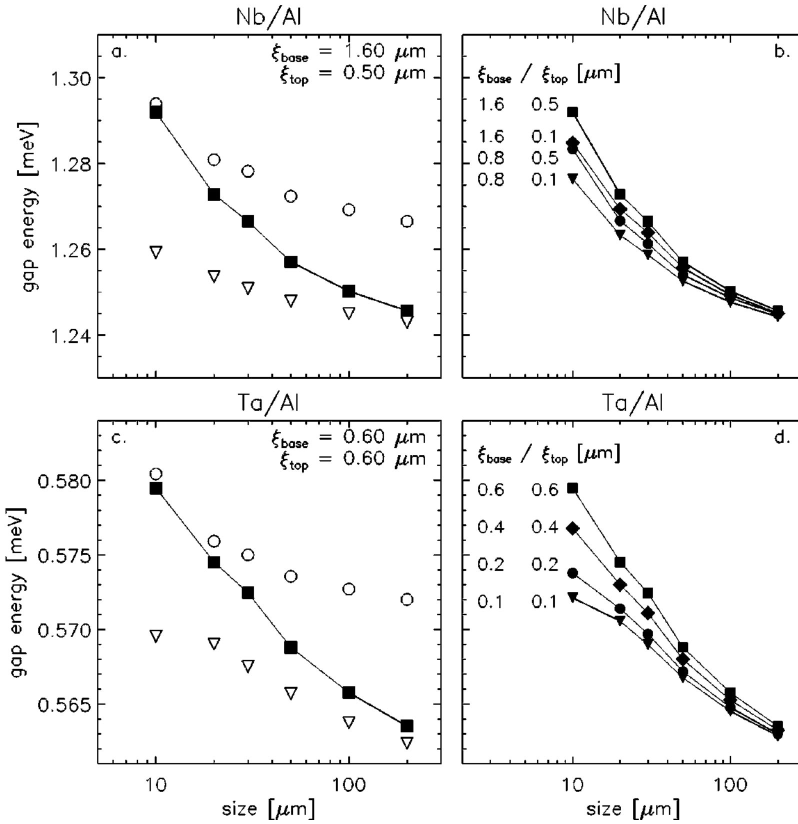

FIG. 9. (a) Computed relations between energy gap and STJ size, for Nb/Al STJ's with $\gamma_m = 0.3$ and $\gamma_B = 0.6$ and the maximum values for the lateral coherence lengths. Triangles indicate the strength of the relation if only the breakdown of superconductivity in the leads played a role. Circles indicate the relation when the breakdown effect is ignored, and only the positional variation of the tunnel current played a role. Squares represent the computations that include all effects. (b) Various ratios of the lateral coherence lengths on either side of the barrier. (c) and (d) Idem, but now for Ta/Al STJ's. The input parameters are $\gamma_m = 0.1$ and $\gamma_B = 0.3$.

is clear from a comparison between the various curves in Figs. 9(b) and the results in Fig. 3.

A similar conclusion is reached for the Ta/Al STJ's. These differ from the Nb-based STJ's in that the Al layers are polycrystalline on either side of the barrier. Therefore the lateral coherence lengths are taken equal in both electrodes. The input parameters are $\gamma_m = 0.1$ and $\gamma_B = 0.3$, as discussed in Sec. III. With this choice of parameters the energy gap is at the level of the average of the three samples in series 2 in Fig. 4. Again, as is apparent in Fig. 9(d), the largest values for ξ_y are required to explain the full gradient in measured energy gaps as a function of STJ size.

At first sight such large values for the lateral coherence length may seem difficult to reconcile with the thickness of the Al layer in the Nb/Al junctions (5–10 nm). The layers below the AlO_x barrier are epitaxial with the monocrystalline sapphire substrate, and are therefore of a high crystallographic quality. On would therefore expect the transport of the electrons through the Al to be dominated by scattering from the barrier and the Nb/Al interface, and the mean free path of the electrons to be of the order of the thickness of the Al layer. However, several workers[43–45] have pointed out that in very thin films the assumption of diffusive scattering may no longer be appropriate. In particular, the fraction of electrons that are reflected specularly becomes appreciable for grazing incidence, provided the interfaces are sufficiently smooth, i.e., do not have features on the scale of the Compton wavelengths of the electrons. Because of the low incidence angles, these electrons will also not be able to tunnel across either of the interfaces. Hence the coherence length of this population may approach the bulk value.

The situation in the Al above the barrier in the Nb STJ's, and in both the electrodes of the Ta-based STJ's, is slightly more complicated. Here the electrons that travel in a lateral direction encounter on average every 50 nm a boundary of a columnar grain. On TEM cross sections these grain boundaries appear to be smooth, even on atomic scales, so it is not very likely that the electrons are diffusively scattered by one encounter. Dispersion of the electrons upon crossing the boundary between two different crystallographic orientations of the Al seems more plausible, given the nonspherical shape of the Fermi surface. Hence the mean-free path of the electrons could easily be several times the diameter of the columnar grains. In fact, we assume it here to be ten times the grain diameter. As is clear from Figs. 9(b) and (d), the effect does not depend on the precise values of ξ_y, but on their order of magnitude.

V. SUMMARY

In the experiments discussed in this paper evidence was found for lateral gradients in the effective energy gap Δ_{gap} of thin films on length scales of (at least) several μm. These gradients were caused by an undercut in the edge of STJ's which caused the outer rim of the Nb or Ta electrodes to become disconnected from the Al proximity layers. In absence of this undercut there was no appreciable relation between Δ_{gap} and STJ size. It was excluded that this effect is only an artifact of the measurement techniques although we identified a mechanism that enhances the effect. The results of these experiments can be understood in terms of a two-dimensional proximity model, which is an extension of the

current proximity models based on Usadel's equations. A remarkable feature of this two-dimensional proximity model is that the lateral part can be separated from the transverse part. Associated with the lateral part is a lateral coherence length ξ_y, which has to be of the order of the bulk coherence length in Al, in order to explain the measurements. This implies that in thin films, the coherence length is not an isotropic quantity. We argued that in thin films, such as the Al layers, large electronic mean free paths in lateral directions are not implausible, even in polycrystalline films. The lateral part of the theory can be recast in a form analogous to Usadel's one-dimensional equation. This form features an effective coherence length $\xi_{\rm eff}$, which depends on quasiparticle energy. For energies close to the gap, it may be an order of magnitude larger than ξ_y, which essentially explains how the measured energy gap of a 50-μm-large STJ is influenced by a feature at the edge.

ACKNOWLEDGMENTS

We gratefully acknowledge the support of H. Zandbergen of the Technical University of Delft, NL, and A. C. Wright of the NEWI in Wrexham, U.K., with the production of the TEM images. We thank A. Kozorezov and K. Wigmore of Lancaster University for stimulating discussions in an earlier stage of this project. All junctions discussed in this paper were produced by the Oxford Instruments Scientific Research Division, Cambridge, U.K. Finally, Aurora BV, Sassenheim, NL, provided financial support.

[1] P. G. De Gennes, Rev. Mod. Phys. **36**, 225 (1964).

[2] A. F. Volkov, A. F. N. Allsopp, and C. J. Lambert, J. Phys.: Condens. Matter **8**, L45 (1996).

[3] Yu. V. Nazarov and T. H. Stoof, Phys. Rev. Lett. **76**, 823 (1996).

[4] H. Courtois, Ph. Gandit, D. Mailly, and B. Pannetier, Phys. Rev. Lett. **76**, 130 (1996).

[5] S. Gueron, H. Pothier, N. O. Birge, D. Esteve, and M. H. Devoret, Phys. Rev. Lett. **77**, 3025 (1996).

[6] K. Neurohr, A. A. Golubov, Th. Klocke, J. Kaufmann, Th. Shaeppers, J. Appenzeller, D. Uhlisch, A. V. Ustinov, M. Hollfelder, H. Lüth, and A. I. Braginski, Phys. Rev. B **54**, 17 018 (1996).

[7] A. Zaitsev and D. Averin, Phys. Rev. Lett. **80**, 3602 (1998).

[8] F. K. Wilhelm, G. Schoen, and A. D. Zaikin, Phys. Rev. Lett. **81**, 1682 (1998).

[9] E. V. Bezuglyi, E. N. Bratus, V. S. Shumeiko, and G. Wendin, Phys. Rev. Lett. **83**, 2050 (1998).

[10] J. J. A. Baselmans, A. F. Morpurgo, B. J. van Wees, and T. M. Klapwijk, Nature (London) **397**, 45 (1999).

[11] A. Shelankov and M. Ozana, Phys. Rev. B **61**, 7077 (2000).

[12] A. Brinkman and A. A. Golubov, Phys. Rev. B **61**, 11 297 (2000).

[13] C. W. J. Beenakker, Rev. Mod. Phys. **69**, 731 (1997).

[14] C. J. Lambert and R. Raimondi, J. Phys.: Condens. Matter **10**, 901 (1998).

[15] W. Belzig, F. K. Wilhelm, C. Bruder, G. Schoen, and A. D. Zaikin, Superlattices Microstruct. **25**, 1251 (1999).

[16] A. A. Golubov, E. P. Houwman, J. P. Gijsbertsen, V. M. Krasnov, J. Flokstra, H. Rogalla, and M. Yu. Kupriyanov, Phys. Rev. B **51**, 1073 (1995).

[17] A. M. Martin and C. J. Lambert, J. Phys.: Condens. Matter **8**, L731 (1996).

[18] A. Poelaert, Ph.D. thesis, Twente University, 1999.

[19] J. M. Martinis, G. C. Hilton, K. D. Irwin, and D. A. Wollman, Nucl. Instrum. Methods Phys. Res. A **444**, 23 (2000).

[20] M. Yu. Kupriyanov, Sov. J. Supercond. **2**, 5 (1992).

[21] M. L. van den Berg, F. B. Kiewiet, M. P. Bruijn, O. J. Luiten, P. A. J. de Korte, J. Martin, and R. P. Huebener, *Proceedings of ASC '98* [IEEE Trans. Appl. Supercond. **9**, 2951 (1999)].

[22] K. Segall, S. Friedrich, C. M. Wilson, D. E. Prober, A. E. Szymkowiak, and S. H. Moseley, *Proceedings of LTD-7, Munich* (Max Planck Institute of Physics, Munich, 1997), p. 47.

[23] S. Friedrich, K. Segall, M. C. Gaidis, C. M. Wilson, D. E. Prober, A. E. Szymkowiak, and S. H. Moseley, Appl. Phys. Lett. **71**, 3901 (1997).

[24] H. Kraus, F. von Feilitzsch, J. Jochum, R. L. Mössbauer, Th. Peterreins, and F. Pröbst, Phys. Lett. B **231**, 195 (1989).

[25] R. den Hartog *et al.*, Proc. SPIE **4012**, 237 (2000).

[26] P. Verhoeve, S. Kraft, N. Rando, A. Peacock, A. van Dordrecht, R. den Hartog, D. J. Goldie, R. Hart, and D. Glowacka, IEEE Trans. Appl. Supercond. **9**, 3342 (1999).

[27] A. Peacock, P. Verhoeve, N. Rando, C. Erd, M. Bavdaz, B. G. Taylor, and D. Perez, Astron. Astrophys., Suppl. Ser. **123**, 581 (1997).

[28] A. Peacock, P. Verhoeve, N. Rando, A. van Dordrecht, B. G. Taylor, C. Erd, M. A. C. Perryman, R. Venn, J. Howlett, D. J. Goldie, J. Lumley, and M. Wallis, Nature (London) **381**, 135 (1996).

[29] M. Gurvitch, M. A. Washington, H. A. Huggins, and J. M. Rowell, IEEE Trans. Magn. **MAG-19**, 791 (1983).

[30] J. M. Lumley, R. E. Somekh, J. E. Evetts, and J. H. James, IEEE Trans. Magn. **MAG-21**, 539 (1985).

[31] W. H. Press, S. A. Teukolsky, W. T. Vetterling, and B. P. Flannery, *Numerical Recipes*, 2nd ed. (Cambridge University Press, Cambridge, 1992).

[32] R. den Hartog, P. Verhoeve, A. Peacock, A. Poelaert, and N. Rando, *Proceedings of ASC '98* [IEEE Trans. Appl. Supercond. **9**, 4495 (1999)].

[33] A. Zehnder, Ph. Lerch, S. P. Zhao, Th. Nussbaumer, and E. C. Kirk, Phys. Rev. B **59**, 8875 (1999).

[34] M. Yu. Kupriyanov and V. F. Luckichev, Zh. Eksp. Teor. Fiz. **94**, 139 (1988) [Sov. Phys. JETP **67**, 1163 (1988)].

[35] M. Tinkham, *Superconductivity*, 2nd ed. (McGraw-Hill International, Singapore, 1996), p. 77.

[36] J. Clarke, Phys. Rev. Lett. **28**, 1363 (1972).

[37] M. Tinkham and J. Clarke, Phys. Rev. Lett. **28**, 1366 (1972).

[38] S. B. Kaplan, C. C. Chi, D. N. Langenberg, J. J. Chang, S. Jafarey, and D. J. Scalapino, Phys. Rev. B **14**, 4854 (1976).

[39] P. Verhoeve, N. Rando, J. Verveer, A. Peacock, A. van Dordrecht, P. Videler, M. Bavdaz, D. J. Goldie, T. Lederer, F. Scholze, G. Ulm, and R. Venn, Phys. Rev. B **53**, 809 (1996).

[40] V. Narayanamurti, R. C. Dynes, P. Hu, H. Smith, and W. F.

Brinkman, Phys. Rev. B **18**, 6041 (1978).
[41] J. Martin, S. Lemke, R. Gross, R. P. Huebener, P. Videler, N. Rando, A. Peacock, P. Verhoeve, and F. A. Jansen, Nucl. Instrum. Methods Phys. Res. A **370**, 88 (1996).
[42] M. L. van den Berg, Ph.D. thesis, Utrecht University, 1999.
[43] S. B. Soffer, J. Appl. Phys. **38**, 1710 (1967).
[44] L. A. Falkovsky, J. Low Temp. Phys. **36**, 713 (1979).
[45] D. Movshovitz and N. Wiser, Phys. Rev. B **41**, 10 503 (1990).